Performance Study of Acoustophoretic Microfluidic Silicon-Glass Devices by Characterization of Material- and Geometry-Dependent Frequency Spectra

Garofalo, Fabio; Laurell, Thomas; Bruus, Henrik

Published in:
Physical Review Applied

Link to article, DOI:
10.1103/PhysRevApplied.7.054026

Publication date:
2017

Document Version
Publisher's PDF, also known as Version of record

Performance Study of Acoustophoretic Microfluidic Silicon-Glass Devices by Characterization of Material- and Geometry-Dependent Frequency Spectra

Fabio Garofalo,[1,*] Thomas Laurell,[1,†] and Henrik Bruus[2,‡]

[1]*Department of Biomedical Engineering, Lund University, Ole Römers Väg 3 S-22363, Lund, Sweden*
[2]*Department of Physics, Technical University of Denmark, DTU Physics Building 309, DK-2800 Kongens Lyngby, Denmark*

(Received 11 October 2016; revised manuscript received 25 January 2017; published 31 May 2017)

The mechanical and electrical response of acoustophoretic microfluidic devices attached to an ac-voltage-driven piezoelectric transducer is studied by means of numerical simulations. The governing equations are formulated in a variational framework that, introducing Lagrangian and Hamiltonian densities, is used to derive the weak form for the finite-element discretization of the equations and to characterize the device response in terms of frequency-dependent figures of merit or indicators. The effectiveness of the device in focusing microparticles is quantified by two mechanical indicators: the average direction of the pressure gradient and the amount of acoustic energy localized in the microchannel. Furthermore, we derive the relations between the Lagrangian, the Hamiltonian, and three electrical indicators: the resonance Q value, the impedance, and the electric power. The frequency response of the hard-to-measure mechanical indicators is correlated to that of the easy-to-measure electrical indicators, and, by introducing optimality criteria, it is clarified to which extent the latter suffices to identify optimal driving frequencies as the geometric configuration and the material parameters vary. The latter have been varied by considering both Pyrex and aluminium nitroxide top-lid materials.

DOI: 10.1103/PhysRevApplied.7.054026

I. INTRODUCTION

Based on the combined action of ultrasound waves and the flow of carrier fluids, acoustofluidics has emerged as a useful tool for the manipulation of biofluids and biological suspensions in microfluidic devices. These devices exploit standing acoustic pressure waves that, through the purely mechanical parameters, such as compressibility, density, and size, induce fluid- and particle-specific forces [1–3] leading to acoustophoresis [4]. This phenomenon is the basis of the development of gentle [5,6] and robust methods for concentrating [7], trapping [8], washing [9], aligning [10], and separating cells [11–13]. In order to be used for manipulation purposes, the acoustic pressure wave inside the microchannel must exhibit well-defined pressure nodes and intense pressure fields that effectively attract or repel particles. For these reasons, acoustofluidic devices operate at acoustic resonance frequencies. Because the speed of sound in water is around 1500 m/s and the typical characteristic dimensions of acoustofluidic microchannels range from 200 to 500 μm, it is seen that ultrasound frequencies of about 1.5–2.5 MHz are ideally suited for creating effective resonance conditions in acoustofluidic devices.

Despite the many successful acoustofluidic devices reported in the literature, a fair amount of calibration and fine-tuning is still involved in the design, optimization, and control during experiments, so as to properly identify the optimal working conditions. While an experimental knowledge of the system response with respect to an external actuation source plays a central role in the selection of good operative conditions [14], a better comprehension of the phenomena involved in these devices would free the design and implementation steps from the costly and time-consuming methods currently employed.

Recently, some progress has been made in numerical modeling of ultrasound and elastic waves in microscale acoustofluidic systems including the piezoelectric transducer, the chip as an elastic solid, and the fluid inside the microchannels [15–17]. Studies including the thermoviscous and transient effects inside microchannels have been reported as well [18–20]. The first numerical optimization studies of acoustophoretic devices have also been performed recently, illustrating a procedure to obtain optimal acoustophoretic forces by changing the geometrical parameters of the device [21]. Other studies involve numerical characterization of the acoustic pressure wave in the microchannel and subsequent computation of particle trajectories by means of numerical integration [22–27].

A major problem regarding the numerical optimization of acoustofluidic devices is the lack of rigorous definitions of macroscopic descriptors which (i) characterize the efficiency of acoustophoretic devices for a given electrical

*Corresponding author.
fabio.garofalo@bme.lth.se
†thomas.laurell@bme.lth.se
‡bruus@fysik.dtu.dk

actuation of the piezoelectric transducer and (ii) are accessible both experimentally and numerically. As an example, in Ref. [21], an objective function, i.e., Eq. (17), containing the Gorkov potential and therefore including both the device performance and the particle properties is used to optimize the performance in the space of the parameters. Note that, since the objective function used in Ref. [21] depends on the particle properties, it would be better to speak about separation performance for the X particle rather than device performance. In this paper, we are interested in investigating the device performance, and thus we will introduce indicators that do not take into account the particle properties but instead exclusively pertain to the device characteristics.

Given the relative ease with which the electrical response of the piezoelectric transducers can be measured compared to the acoustophoretic response, it would be advantageous to demonstrate numerically and experimentally a direct correlation between these two responses, such that the hard-to-obtain acoustophoretic response could be inferred from the easy-to-obtain electric response. A first step in this direction was taken in experiments on simple glass capillaries by Hammarström *et al.* [14]. A further complication is the influence of thermal heating by the piezoelectric transducer, which directly affects the acoustic response of the device through the temperature dependence of the acoustic-relevant parameters (density, compressibility, and elastic moduli). However, because an overall temperature increase in an operative device can be easily prevented by including a Peltier cooling element attached to the device [26,28], we choose not to take thermal heating into account in the simulations presented here.

In order to characterize acoustophoretic devices, in this paper, we aim (i) to introduce the descriptors that enable a quantitative analysis of frequency spectra in the case of purely electromechanical interactions of the device with the liquid-filled microchannel, (ii) to provide an easy-to-run two-dimensional model aiming to address the features of a fully three-dimensional device, and (iii) to compare the behavior of different acoustofludic devices as a function of the geometrical and material parameters.

The manuscript is organized as follows. In Sec. II, we (A) define the model device in the form of a microchannel embedded in a silicon substrate with a top lid and a piezoelectric transducer attached to the bottom of the silicon, (B) introduce the governing equations using the Lagrangian and Hamiltonian formalism, (C) formulate the coupling between the various subsystems of the device, (D) introduce the system indicators, and (E) describe the finite-element discretization that constitutes the basis of the numerical simulations. The materials chosen for the top lid, either Pyrex or ALON (aluminium nitroxide [29]) glass, are both transparent, thus allowing for optical access to the microchannel. In Sec. III, we report on the details of the numerical implementation by (A) illustrating the weak form used in the finite-element discretization and (B) validating the model in terms of global and frequency-wise errors and energy consistency. In Sec. IV, we (A) introduce the procedure for identifying optimal acoustophoretic frequencies, (B) perform the mechanical spectral analysis of Pyrex-silicon devices, (C) report on some examples that identify optimal frequencies, (D) perform electric spectral analysis of Pyrex-silicon devices, and (E) introduce and validate a procedure to identify resonance frequencies from the impedance characteristics. In Sec. V, we discuss the results and address possible experimental tests. Finally, in the Appendix, we discuss the meaning of the two-dimensional analysis and the extension of the actual model to a fully three-dimensional numerical model.

II. ACOUSTOPHORETIC-DEVICE MODEL

A. Description of the device

The long and straight acoustophoretic device consists of a piezoelectric transducer underneath a chip. The latter is made of a glass lid on top and a silicon substrate with an embedded microfluidic channel. Figures 1(a) and 1(b) show photographs of actual silicon-glass devices including the chip mounted on the piezoelectric transducer, while Fig. 1(c) shows the cross section of the device defining the computational domain used in the numerical study. The piezoelectric transducer is modeled as a rectangular domain of width w_{pz} and height h_{pz} driven by an ac-voltage difference ϕ_{app} applied between its top and bottom surfaces. The bottom surface is considered fixed, while the side surfaces move freely. The silicon substrate is a rectangular domain of width w_{si} and height h_{si}. The rectangular microfluidic channel of width w_{ch} and height h_{ch} is etched into the top of the silicon substrate. Finally, a rectangular glass lid of width $w_{\mathrm{gl}} = w_{\mathrm{si}}$ and height h_{gl} is placed on top of the silicon substrate. The center line of the piezoelectric transducer is displaced by a distance d_{pz} with respect to the center line of the chip.

B. Governing equations and Lagrangian densities

In the following, we formulate the governing equations and report the free Lagrangian densities for the elastic, acoustic, and piezoelectric waves in the case of a time-harmonic actuation. The material properties are not specified, as we tacitly assume that these are different for different materials (see Sec. III for further details).

1. Elastic waves

The propagation of elastic waves in the silicon chip and the glass lid is governed by the time-dependent Navier equation [30,31],

$$-\rho\partial_t^2\boldsymbol{u} + \boldsymbol{\nabla}\cdot\boldsymbol{\sigma}_{\mathrm{mc}} = \mathbf{0}, \tag{1}$$

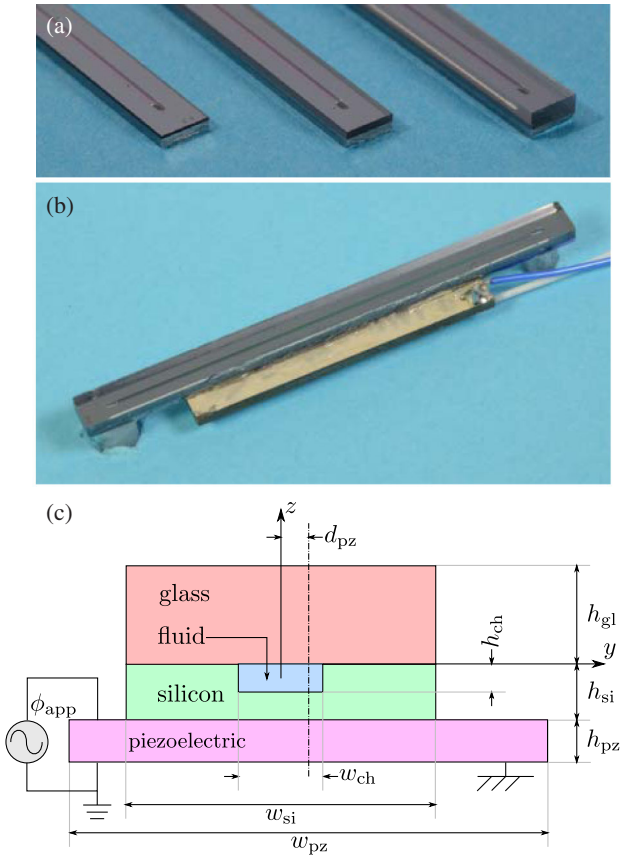

FIG. 1. (a) Photograph of three prototypical acoustophoretic silicon-glass chips with glass lids 0.5, 0.7, and 1.1 mm high, respectively. (b) Photograph of a complete device with a 40-mm-long silicon-glass chip (gray) with short fluidic tubings attached underneath the chip ends and mounted on the piezoelectric transducer (brown) connected by electrical wires (blue and white). (c) The cross section of the device defining the two-dimensional computational domain.

where ρ is the density of the material, $\boldsymbol{u}$ is the displacement, and $\boldsymbol{\sigma}_{\mathrm{mc}}$ is the mechanical stress tensor. The constitutive equation relating the mechanical stress to the displacement in the linear regime is given by [30,32]

$$\boldsymbol{\sigma}_{\mathrm{mc}} = \boldsymbol{\Sigma}:\boldsymbol{\gamma}, \tag{2}$$

where $\boldsymbol{\gamma} = \frac{1}{2}[\boldsymbol{\nabla u} + (\boldsymbol{\nabla u})^T]$ is the strain tensor, $\boldsymbol{\Sigma}$ is the rank-4 stiffness tensor. The superscript T and the colon denote the transpose and the inner product of the tensors, respectively. The stiffness tensor $\boldsymbol{\Sigma}$ has $3^4 = 81$ components, but the positivity of the elastic strain energy, expressed by the constraints $\Sigma_{ij,kl} = \Sigma_{kl,ij}$, $\Sigma_{ij,kl} = \Sigma_{ji,kl}$, and $\Sigma_{ij,kl} = \Sigma_{ij,lk}$, reduces the number of independent components to 21. For monocrystalline silicon, $\boldsymbol{\Sigma}$ is fully described by only three parameters, and two parameters (the Young modulus and the Poisson ratio) suffice for isotropic glass [30–32].

The Navier equation (1) can be written in the frequency domain (Helmholtz form) by using the time-domain Fourier representation $u(\boldsymbol{x}, t) = u(\boldsymbol{x}, \omega)e^{-i\omega t}$,

$$\rho\omega^2\boldsymbol{u} + \boldsymbol{\nabla}\cdot\boldsymbol{\sigma}_{\mathrm{mc}} = \boldsymbol{0}, \tag{3}$$

where $\omega = 2\pi f$ is the angular frequency corresponding to the actuation frequency f of the transducer.

In a variational approach to the field equations [33], Eq. (3) is the Euler-Lagrange equation $\partial\mathcal{L}_{\mathrm{mc}}/\partial\boldsymbol{u}^* - \boldsymbol{\nabla}\cdot[\partial\mathcal{L}_{\mathrm{mc}}/\partial(\boldsymbol{\nabla u}^*)] = \boldsymbol{0}$ derived from the variation of the mechanical Lagrangian $L_{\mathrm{mc}} = \int \mathcal{L}_{\mathrm{mc}} d\boldsymbol{x}$ with

$$\mathcal{L}_{\mathrm{mc}}(\boldsymbol{u}, \boldsymbol{\nabla u}) = \rho\omega^2\boldsymbol{u}^*\cdot\boldsymbol{u} - \boldsymbol{\nabla u}^*:\boldsymbol{\Sigma}:\boldsymbol{\nabla u}, \tag{4}$$

where the asterisk denotes the transposed conjugate. Note that, because $\boldsymbol{\Sigma}$ is symmetric in both pairs of its indices, the inner product $\boldsymbol{\nabla u}^*:\boldsymbol{\Sigma}:\boldsymbol{\nabla u}$ equals $\boldsymbol{\gamma}^*:\boldsymbol{\Sigma}:\boldsymbol{\gamma}$. This rule will be used in the following to disregard the antisymmetric part of the deformation $\boldsymbol{\nabla u}$ when it is double dotted with a symmetric tensor, such as $\boldsymbol{\Sigma}$.

2. Acoustic waves

The governing equation for the acoustic waves in the frequency domain (inviscid fluid) inside the microfluidic channel is the wave equation [34]

$$\kappa_{\mathrm{ac}}p + \frac{1}{\rho\omega^2}\boldsymbol{\nabla}\cdot\boldsymbol{\nabla}p = 0, \tag{5}$$

where ρ is the density of the fluid, $\kappa_{\mathrm{ac}} = [1/(\rho c^2)]$ is its isentropic compressibility, c is the speed of sound (considered complex valued so as to include bulk dissipation), and p is the acoustic pressure. The governing equation can be derived from the acoustic Lagrangian density $\mathcal{L}_{\mathrm{ac}}$ of the fluid,

$$\mathcal{L}_{\mathrm{ac}}(p, \boldsymbol{\nabla}p) = \kappa_{\mathrm{ac}}p^*p - \frac{1}{\rho\omega^2}\boldsymbol{\nabla}p^*\cdot\boldsymbol{\nabla}p. \tag{6}$$

Note that (i) the factor ω^2 in Eq. (5) appears in such a way that the Lagrangian $\mathcal{L}_{\mathrm{ac}}$ has the dimension of an energy density, the same as $\mathcal{L}_{\mathrm{mc}}$, and (ii) the role of the kinetic and potential energies in $\mathcal{L}_{\mathrm{ac}}$ is reversed when compared to $\mathcal{L}_{\mathrm{mc}}$ since, in acoustics, the potential energy is the p^*p term and the kinetic energy is the gradient-product term [34–36].

3. Piezoelectric waves

The governing equations in the linear deformation regime for the electromechanical (em) or piezoelectric waves in the piezoelectric transducer are the Helmholtz-Navier equation (3) coupled with the conservation for the electric displacement $\boldsymbol{d}_{\mathrm{em}}$ in the absence of an electric charge distribution [37],

$$\rho\omega^2\boldsymbol{u} + \boldsymbol{\nabla}\cdot\boldsymbol{\sigma}_{\mathrm{em}} = \boldsymbol{0}, \tag{7a}$$

$$\boldsymbol{\nabla}\cdot\boldsymbol{d}_{\mathrm{em}} = \boldsymbol{0}, \tag{7b}$$

where $\boldsymbol{\sigma}_{\mathrm{em}}$ is the electromechanical stress tensor and $\boldsymbol{d}_{\mathrm{em}}$ is the electric displacement vector. The linear stress-charge constitutive equations [37] for $\boldsymbol{\sigma}_{\mathrm{em}}$ and $\boldsymbol{d}_{\mathrm{em}}$ are extensions of Eq. (2) and the standard constitutive relation for the electric displacement,

$$\boldsymbol{\sigma}_{\mathrm{em}} = \boldsymbol{\Sigma} : \boldsymbol{\gamma} + \boldsymbol{P}^{\dagger} \cdot \boldsymbol{\nabla}\phi, \tag{8a}$$

$$\boldsymbol{d}_{\mathrm{em}} = \boldsymbol{P} : \boldsymbol{\gamma} - \boldsymbol{\varepsilon} \cdot \boldsymbol{\nabla}\phi, \tag{8b}$$

where ϕ is the electrostatic potential and $\boldsymbol{\varepsilon}$ is the dielectric permittivity tensor. The piezoelectric coupling tensor $\boldsymbol{P}$ is a rank-3 tensor that is symmetric in its rightmost indices, $P_{i,jk} = P_{i,kj}$, and where $[\boldsymbol{P}^{\dagger}]_{kj,i} = [\boldsymbol{P}]^{*}_{i,jk}$ is the Hermitian conjugate. These symmetries imply that $\boldsymbol{P}:\boldsymbol{\gamma} = \boldsymbol{P}:\boldsymbol{\nabla u}$. Finally, the corresponding Lagrangian density $\mathcal{L}_{\mathrm{em}}$ is

$$\begin{aligned}\mathcal{L}_{\mathrm{em}}(\boldsymbol{u}, \boldsymbol{\nabla u}, \phi, \boldsymbol{\nabla}\phi) = {} & \rho\omega^2 \boldsymbol{u}^{*} \cdot \boldsymbol{u} - \boldsymbol{\nabla u}^{*} : \boldsymbol{\Sigma} : \boldsymbol{\nabla u} \\ & - \boldsymbol{\nabla}\phi^{*} \cdot \boldsymbol{P} : \boldsymbol{\nabla u} - \boldsymbol{\nabla u}^{*} : \boldsymbol{P}^{\dagger} \cdot \boldsymbol{\nabla}\phi \\ & + \boldsymbol{\nabla}\phi^{*} \cdot \boldsymbol{\varepsilon} \cdot \boldsymbol{\nabla}\phi,\end{aligned} \tag{9}$$

which is similar to that provided by Ref. [37] (see the discussion and table in Sec. 1.2) for the static case, except for the fact that the kinetic term, i.e., $\rho\omega^2 \boldsymbol{u}^{*} \cdot \boldsymbol{u}$, has been included.

C. Boundary conditions

The boundary conditions for the above-mentioned four domains (piezoelectric transducer, silicon chip, water channel, and glass lid) are set as follows.

Mechanically, the piezoelectric transducer is free to vibrate (zero stress) at the bottom wall $S_{\mathrm{pz/bot}}$ and at the interface $S_{\mathrm{pz/air}}$, while the displacement and the stress are continuous across the interface $S_{\mathrm{pz/si}}$ with the silicon chip,

$$\boldsymbol{\sigma}_{\mathrm{em}} \cdot \hat{\boldsymbol{n}} = \boldsymbol{0}, \qquad \boldsymbol{x} \in S_{\mathrm{pz/bot}}, \tag{10a}$$

$$\boldsymbol{\sigma}_{\mathrm{em}} \cdot \hat{\boldsymbol{n}} = \boldsymbol{0}, \qquad \boldsymbol{x} \in S_{\mathrm{pz/air}}, \tag{10b}$$

$$[\![\boldsymbol{u}]\!] = \boldsymbol{0} \quad \text{and} \quad [\![\boldsymbol{\sigma}]\!] \cdot \hat{\boldsymbol{n}} = \boldsymbol{0}, \qquad \boldsymbol{x} \in S_{\mathrm{pz/si}}, \tag{10c}$$

where $[\![g]\!] = g_2 - g_1$ is the difference in g across an interface separating 2 from 1 [note that the stress in the piezoelectric transducer is $\boldsymbol{\sigma}_{\mathrm{em}}$ as defined in Eq. (9), while in the silicon, it is $\boldsymbol{\sigma}_{\mathrm{mc}}$ as defined in Eq. (2)]. Electrically, the piezoelectric transducer has zero potential at the bottom wall $S_{\mathrm{pz/bot}}$, an externally applied potential ϕ_{app} on the top wall $S_{\mathrm{pz/top}}$, and zero surface charge on the side walls $S_{\mathrm{pz/side}}$,

$$\phi = 0, \qquad \boldsymbol{x} \in S_{\mathrm{pz/bot}}, \tag{11a}$$

$$\phi - \phi_{\mathrm{app}} = 0, \qquad \boldsymbol{x} \in S_{\mathrm{pz/top}}, \tag{11b}$$

$$\boldsymbol{d}_{\mathrm{em}} \cdot \hat{\boldsymbol{n}} = 0, \qquad \boldsymbol{x} \in S_{\mathrm{pz/side}}. \tag{11c}$$

Given the linearity of the model presented here, we can assume, without loss of generality, that the applied voltage is $\phi_{\mathrm{app}} = 1$ V (for real-world devices, this voltage is usually between 3 and 7 V).

The remaining boundary conditions are purely mechanical. The glass and silicon surfaces exposed to air ($S_{\mathrm{gl/air}}$ and $S_{\mathrm{si/air}}$) have zero stress and the silicon-glass interface ($S_{\mathrm{si/gl}}$) has a continuous displacement field and stress tensor, while the glass and silicon surfaces ($S_{\mathrm{gl/fl}}$ and $S_{\mathrm{si/fl}}$) exposed to the fluid in the microchannel have continuous stress (the tangential stress in the inviscid fluid is, by definition, zero) and normal displacement,

$$\boldsymbol{\sigma} \cdot \hat{\boldsymbol{n}} = \boldsymbol{0}, \quad \boldsymbol{x} \in S_{\mathrm{si/air}}, \quad S_{\mathrm{gl/air}}, \tag{12a}$$

$$[\![\boldsymbol{u}]\!] = \boldsymbol{0} \ \text{ and } \ [\![\boldsymbol{\sigma}]\!] \cdot \hat{\boldsymbol{n}} = \boldsymbol{0}, \quad \boldsymbol{x} \in S_{\mathrm{si/gl}}, \tag{12b}$$

$$[\![\boldsymbol{u}]\!] \cdot \hat{\boldsymbol{n}} = 0 \ \text{ and } \ [\![\boldsymbol{\sigma}]\!] \cdot \hat{\boldsymbol{n}} = \boldsymbol{0}, \quad \boldsymbol{x} \in S_{\mathrm{si/fl}}, \quad S_{\mathrm{gl/fl}}. \tag{12c}$$

Note that, for the fluid, the displacement field is given by $\boldsymbol{u}_{\mathrm{fl}} = [1/(\rho\omega^2)]\boldsymbol{\nabla} p$ and the stress by $\boldsymbol{\sigma}_{\mathrm{fl}} = -p\mathbf{1}$, where $\mathbf{1}$ is the unit tensor.

So far, the boundary conditions have been expressed in their strong forms. However, for the numerical implementation in the finite-element method, we need to formulate them in weak form, and adding the contributions so obtained to the free Lagrangian density equations (4), (6), and (9) leads to correctly constrained solutions to the variational problem.

The boundary terms for the free Lagrangian densities $\mathcal{L}_{\mathrm{mc}}$, $\mathcal{L}_{\mathrm{ac}}$, and $\mathcal{L}_{\mathrm{em}}$ are derived from the virtual work form of Eqs. (3), (5), and (8) by considering integration over the relevant domain and application of the Green-Gauss theorem. This operation yields the sought-after contributions in terms of the surface-normal component of the fluxes,

$$\mathcal{L}^{\mathrm{bnd}}_{\mathrm{mc}}(\boldsymbol{u}, \boldsymbol{\sigma}^{\mathrm{bnd}}_{\mathrm{mc}}) = \boldsymbol{u}^{*} \cdot \boldsymbol{\sigma}^{\mathrm{bnd}}_{\mathrm{mc}} \cdot \hat{\boldsymbol{n}}, \tag{13a}$$

$$\mathcal{L}^{\mathrm{bnd}}_{\mathrm{ac}}(p, \boldsymbol{u}^{\mathrm{bnd}}_{\mathrm{fl}}) = p^{*} \boldsymbol{u}^{\mathrm{bnd}}_{\mathrm{fl}} \cdot \hat{\boldsymbol{n}}, \tag{13b}$$

$$\mathcal{L}^{\mathrm{bnd}}_{\mathrm{em}}(\boldsymbol{u}, \boldsymbol{\sigma}^{\mathrm{bnd}}_{\mathrm{em}}, \phi, \boldsymbol{d}^{\mathrm{bnd}}_{\mathrm{em}}) = \boldsymbol{u}^{*} \cdot \boldsymbol{\sigma}^{\mathrm{bnd}}_{\mathrm{em}} \cdot \hat{\boldsymbol{n}} - \phi^{*} \boldsymbol{d}^{\mathrm{bnd}}_{\mathrm{em}} \cdot \hat{\boldsymbol{n}}, \tag{13c}$$

where the reaction forces—the dot product of the fluxes with the surface normal $\hat{\boldsymbol{n}}$—are explicitly addressed. At interfaces between neighboring domains, these contributions cancel due to the presence of surface normals that have opposite direction in the two domains. Therefore, if no extra surface contribution is added to the Lagrange densities, the continuity condition $[\![\cdot]\!] = 0$ for the normal

fluxes at such interfaces is automatically fulfilled. For free boundaries such as external walls, the reaction forces are, by definition, zero, and if no further terms are added to the Lagrangian, these boundary conditions are also fulfilled.

On the bottom wall of the piezoelectric transducer, the Dirichlet condition on the electrical potential ϕ is imposed using the standard method of Lagrange multiplier functions: here, μ_{em}. This method amounts to adding the following Lagrange surface-density contribution,

$$\mathcal{L}_{\mathrm{em}}^{\mathrm{bot}} = \phi^* \mu_{\mathrm{em}} + \mu_{\mathrm{em}}^* (-\phi), \tag{14}$$

to the free Lagrange mechanical density $\mathcal{L}_{\mathrm{em}}$, through which we obtain the Euler-Lagrange equation $\partial_{\mu_{\mathrm{em}}^*} \mathcal{L}_{\mathrm{em}}^{\mathrm{bot}} = 0$, which implies $\phi = 0$. Similarly, for the piezoelectric top wall we add the following Lagrange surface density $\mathcal{L}_{\mathrm{em}}^{\mathrm{top}}$ to the free Lagrange mechanical density:

$$\mathcal{L}_{\mathrm{em}}^{\mathrm{top}} = \phi^* \mu_{\mathrm{em}} + \mu_{\mathrm{em}}^* (-\phi + \phi_{\mathrm{app}}). \tag{15}$$

The Euler-Lagrange equation for μ_{em}^* leads to the correct boundary condition, $\phi = \phi_{\mathrm{app}} e^{-i\omega t}$, on the top wall.

By using the virtual work theorem and the Gauss's theorem, it is straightforward to prove that the total work $\hat{W}(\omega) = \int_{S_{\mathrm{top}}} \mathcal{W}(\boldsymbol{x}, \omega) dS$ made by the external actuation source on the acoustofluidic device equals the volume integral over the system domain Ω of the total Lagrange density $\mathcal{L} = \mathcal{L}_{\mathrm{mc}} + \mathcal{L}_{\mathrm{ac}} + \mathcal{L}_{\mathrm{em}}$,

$$\hat{W}(\omega) = \int_{\Omega} \mathcal{L}(\boldsymbol{x}, \omega) d\boldsymbol{x}. \tag{16}$$

Henceforth, we use the hat notation on capital letters to denote complex-valued integral quantities such as $\hat{W}(\omega)$.

D. Definition of system indicators

From the Lagrangian densities introduced in the previous section, we can derive the expressions for the Hamiltonian densities, the stored energy, and the dissipated power for the device. By using complex notation and treating a field $\boldsymbol{q}$ and its complex conjugate $\boldsymbol{q}^*$ as independent variables, the corresponding Hamiltonian density is given by $\mathcal{H} = \boldsymbol{q}^* \cdot [\partial \mathcal{L} / (\partial \boldsymbol{q}^*)] + \boldsymbol{q} \cdot [\partial \mathcal{L} / (\partial \boldsymbol{q})] - \mathcal{L}$. This prescription results in the following three Hamiltonian densities for each of the three subsystems:

$$\mathcal{H}_{\mathrm{mc}} = \rho \omega^2 \boldsymbol{u}^* \cdot \boldsymbol{u} + \boldsymbol{\nabla u}^* : \boldsymbol{\Sigma} : \boldsymbol{\nabla u}, \tag{17a}$$

$$\mathcal{H}_{\mathrm{ac}} = \kappa_{\mathrm{ac}} p^* p + \frac{1}{\rho \omega^2} \boldsymbol{\nabla} p^* \cdot \boldsymbol{\nabla} p, \tag{17b}$$

$$\begin{aligned} \mathcal{H}_{\mathrm{em}} = {} & \rho \omega^2 \boldsymbol{u}^* \cdot \boldsymbol{u} + \boldsymbol{\nabla u}^* : \boldsymbol{\Sigma} : \boldsymbol{\nabla u} - \boldsymbol{\nabla} \phi^* \cdot \boldsymbol{\varepsilon} \cdot \boldsymbol{\nabla} \phi \\ & + \boldsymbol{\nabla} \phi^* \cdot \boldsymbol{P} : \boldsymbol{\nabla u} - \boldsymbol{\nabla u}^* : \boldsymbol{P}^{\dagger} \cdot \boldsymbol{\nabla} \phi. \end{aligned} \tag{17c}$$

Note that, to interpret the quantities introduced in Eq. (17) as energies, the real part of these quantities must be positive. This constraint (i) implies constraints on the actual material parameters (in terms of numerical values and symmetries of the higher-rank tensor) and (ii) provides a further method to check the energy consistency of the model presented here.

The quadratic structure of the Hamiltonian densities implies that, for a given domain $n = \mathrm{pz}$, si, gl, or ch, the contribution $H_n(\omega)$ to the total energy of the system is given by the time average over one oscillation period of the integrated complex-valued Hamiltonian $\hat{H}_n(\omega)$ as

$$H_n(\omega) = \frac{1}{2} \mathrm{Re}[\hat{H}_n(\omega)], \tag{18a}$$

$$\hat{H}_n(\omega) = \int_{\Omega_n} \mathcal{H}_n(\boldsymbol{x}, \omega) d\boldsymbol{x}, \qquad n = \mathrm{pz}, \mathrm{si}, \mathrm{gl}, \mathrm{ch}. \tag{18b}$$

The total energy per cycle $H(\omega)$ of the system is thus

$$H(\omega) = H_{\mathrm{pz}}(\omega) + H_{\mathrm{si}}(\omega) + H_{\mathrm{si}}(\omega) + H_{\mathrm{ch}}(\omega). \tag{19}$$

As described in Eq. (15), the system is driven by the applied potential $\phi = \phi_{\mathrm{app}} e^{-i\omega t}$ on the top wall of the piezoelectric transducer. The dissipated power $P(\omega)$ is thus given by the time average over one period of the complex-valued rate $\hat{P} = -i\omega \hat{W}(\omega)$ of the applied work $\hat{W}(\omega)$ given in Eq. (16),

$$P(\omega) = \frac{1}{2} \mathrm{Re}[\hat{W}(\omega)] = \frac{\omega}{2} \mathrm{Im}[\hat{L}(\omega)], \tag{20}$$

where the total complex-valued Lagrangian $\hat{L}(\omega)$ of the system in analogy with the Hamiltonian is given by

$$\hat{L}(\omega) = \hat{L}_{\mathrm{pz}}(\omega) + \hat{L}_{\mathrm{si}}(\omega) + \hat{L}_{\mathrm{si}}(\omega) + \hat{L}_{\mathrm{ch}}(\omega), \tag{21a}$$

$$\hat{L}_n(\omega) = \int_{\Omega_n} \mathcal{L}_n(\boldsymbol{x}, \omega) d\boldsymbol{x}, \qquad n = \mathrm{pz}, \mathrm{si}, \mathrm{gl}, \mathrm{ch}. \tag{21b}$$

An important indicator for characterizing the system in terms of electric measurements is the complex-valued electrical impedance $\hat{Z}(\omega)$ defined through the voltage-current relation $\phi_{\mathrm{app}} = \hat{Z} \hat{I}$. Multiplying this expression by ϕ_{app}^* and recalling that the dissipated power is given by $\hat{P} = \phi_{\mathrm{app}}^* \hat{I} = -i\omega \hat{L}$, we obtain the electrical impedance,

$$\hat{Z}(\omega) = i \frac{|\phi_{\mathrm{app}}|^2}{\omega \hat{L}(\omega)}, \qquad \hat{Z} = Z(\omega) \exp[i \varphi_Z(\omega)], \tag{22}$$

where Z is the absolute value of the impedance and φ_Z is the phase. Since $\hat{L}(\omega)$ depends quadratically on the applied potential, we note that, as expected, the electrical

impedance is independent of ϕ_{app}. Below, we investigate to which extent the electrical impedance, which is easy to measure, characterizes the acoustic part of the electromechanical resonances of the system.

Additionally, from the total Hamiltonian $H(\omega)$ and the dissipated power $P(\omega)$, one can calculate the quality factor, or Q value, for the electrically driven acoustofluidic device as [38]

$$Q(\omega) = \frac{\omega H(\omega)}{P(\omega)} = \frac{\mathrm{Re}[\hat{H}(\omega)]}{\mathrm{Im}[\hat{L}(\omega)]}. \tag{23}$$

The Q value is one of the indicators used to characterize acoustofluidic chips; indeed, high Q values indicate strong and well-defined resonances of the system. However, we drop the use of this Q in favor of an electric characterization based on the impedance equation (22).

The above indicators characterize the system in its entirety. An indicator addressing indirectly the amount of radiation force the system is capable of producing within the microchannel is the fraction η of the total energy $H(\omega)$ that resides as acoustic energy $H_{\text{ch}}(\omega)$ in the channel,

$$\eta(\omega) = \frac{H_{\text{ch}}(\omega)}{H(\omega)}. \tag{24}$$

Indeed, the acoustic radiation force responsible for the acoustophoresis in the channel is proportional to H_{ch} [1], and thus to η. As η approaches unity, the acoustic radiation force in the fluid attains the maximum radiation force achievable for a device, as all of the energy is stored as acoustic energy in the fluid. According to this property, η can be termed the *acoustofluidic yield*.

However, the acoustofluidic yield quantifies only the magnitude of the acoustophoretic forces. To obtain good acoustophoresis—say, particle separation—the direction of these forces also needs to be optimal. To quantify the optimal directionality, we introduce the *acoustophoretic mean orientation* $\theta(\omega)$, defined in terms of the sine of the average direction of the pressure gradient,

$$\theta(\omega) = \sin\left(\arctan\frac{\|\partial_y p(\boldsymbol{x},\omega)\|}{\|\partial_z p(\boldsymbol{x},\omega)\|}\right). \tag{25}$$

Here, the average $\|f(\boldsymbol{x})\|$ of a field $f(\boldsymbol{x})$ is defined as the average of the absolute value $|f(\boldsymbol{x})|$ in the channel domain Ω_{ch}.

Good acoustophoresis—namely, focusing by horizontal motion towards the vertical center plane—is obtained when the average of the horizontal pressure gradient $\|\partial_y p\|$ is much larger than the vertical one $\|\partial_z p\|$. For example, in the ideal case of a horizontal standing pressure half wave, $p(\boldsymbol{x}) = p_0\cos\{\pi[y/(w_{\text{ch}})]\}$, we obtain $\partial_z p = 0$, and thus $\theta = 1$. By contrast, a dominating vertical gradient corresponding to $\theta = 0$ is useless. The acoustophoretic mean orientation θ contains only information about the direction of the pressure wave. If information is required about other features of the pressure field (number and distribution of the nodes and/or spatial homogeneity), additional indicators must be introduced. For the analysis presented below, the use of θ suffices.

It must be noted that the acoustophoretic mean orientation is based on the assumption that the dipole scattering coefficient in the Gorkov potential [2] equals zero since the definition equation (25) takes into account only the gradient of the pressure field. This is a good approximation when the acoustophoretic separation involves cells suspended in aqueous media, as the cell density is usually quite close to water density, almost canceling the contribution of the dipole scattering coefficient.

III. NUMERICAL IMPLEMENTATION

A. Finite-element discretization

The Lagrangian representation introduced in Sec. II B and the corresponding boundary contributions in Sec. II C are suitable for implementing numerical simulations with the finite-element method. The numerical simulations are performed using the finite-element software COMSOL [39]. The coarse mesh shown in Fig. 2 is generated by COMSOL. A finer mesh is used in the actual simulations and generated by assuming the geometric parameters in Table I.

The Lagrangian densities (4), (6), and (9) corresponding to the governing equations (3), (5), and (7) are implemented in COMSOL by substituting the complex-conjugate fields $\boldsymbol{u}^*$, p^*, and ϕ^* by the so-called test functions $\boldsymbol{u}^\dagger$, $p^\dagger$, and $\phi^\dagger$. For the sake of clarity, an overview of the weak-form implementation in COMSOL is shown in the block diagram of Fig. 3. The larger boxes in the diagram contain the subdomain bulk equations of Sec. II B, while the boundary conditions of Sec. II C are displayed in the smaller boxes, from which arrows point to the interfaces (the dashed regions), where they have been applied. The condition equations (12c) are implemented by the substitutions

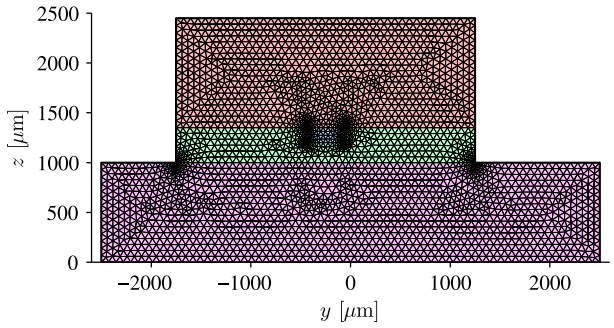

FIG. 2. Example of a mesh generated in the computational domain defined in Fig. 1 with a mesh resolution $m_{\text{res}} = 0.35$; see the details in Sec. III B. The geometry parameters are listed in Table I. Specifically, the glass-lid height is $h_{\text{gl}} = 1100$ μm and the displacement is $d_{\text{pz}} = 250$ μm.

TABLE I. List of the geometry parameters for glass, silicon, channel and Pz26 used in the simulations.

Length	Symbol	Value
Glass height	h_{gl}	200, 500, 700, 1100 μm
Glass width	w_{gl}	375 μm
Silicon height	h_{si}	350 μm
Silicon width	w_{si}	3000 μm
Channel height	h_{ch}	150 μm
Channel width	w_{ch}	375 μm
Pz26 height	h_{pz}	1000 μm
Pz26 width	w_{pz}	5000 μm
Pz26 displacement	d_{pz}	0, 250, 500 μm

$\boldsymbol{\sigma}_s \to -p_f\mathbf{1}$ in $\mathcal{L}_{mc}^{bnd}$ and $\boldsymbol{u}_{fl} \to \boldsymbol{u}_{sl}$ in $\mathcal{L}_{fl}^{bnd}$. Tables I and II contain the geometrical and material parameters used in the simulations.

B. Model validation

We perform a number of tests to demonstrate the reliability of the numerical simulations for frequencies which, as explained in Sec. IV, lie between 1.5 and 2.5 MHz. First, we conduct a mesh-convergence analysis choosing a Pyrex lid $h_{gl} = 1100$ μm high and a centered piezoelectric transducer ($d_{pz} = 0$ μm). We use meshes of triangular elements with a coarseness controlled by a mesh

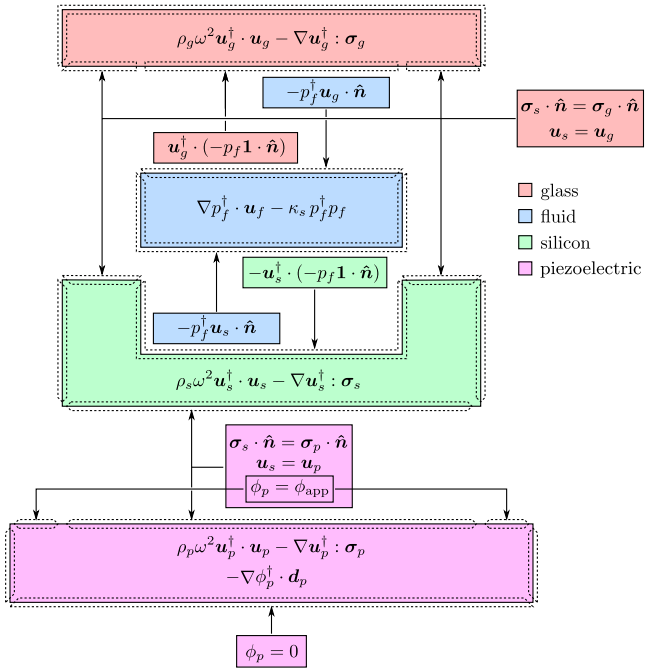

FIG. 3. Block diagram illustrating the weak-form implementation of the bulk equations of Sec. II B (larger boxes) and the boundary conditions of Sec. II C (smaller boxes). The system is driven by the applied potential ϕ_{app} at angular frequency ω. The fields are displacement $\boldsymbol{u}$, stress $\boldsymbol{\sigma}$, pressure p, electric potential ϕ, and electric displacement $\boldsymbol{d}$. The material parameters are listed in Table II. The subscripts refer to the subdomains.

TABLE II. List of the material parameters used in the simulations. We assume that $Q_{si} = \infty$ and $Q_{al} = Q_{Py}$.

Parameter	Symbol and value
Water parameters: [19,21]	
Speed of sound	$c_{wa} = (1 + i\frac{1}{2}\varphi_{wa})1481$ m s^{-1}
Density	$\rho_{wa} = 998$ kg m^{-3}
Loss factor	$\varphi_{wa} = 0.01$
Pyrex parameters: [40]	
Density	$\rho_{Py} = 2220$ kg m^{-3}
Young modulus	$E_{Py} = \{1 + i[1/(Q_{Py})]\}63$ GPa
Poisson ratio	$\nu_{Py} = 0.2$
Quality factor	$Q_{Py} = 1250$
ALON parameters: [29]	
Density	$\rho_{al} = 3688$ kg m^{-3}
Young modulus	$E_{al} = \{1 + i[1/(Q_{al})]\}334$ GPa
Poisson ratio	$\nu_{al} = 0.239$
Quality factor	$Q_{al} = 1250$
Silicon parameters: [17,41]	
Density	$\rho_{si} = 2330$ kg m^{-3}
Stiffness matrix	$\boldsymbol{\Sigma}_{si} = \boldsymbol{\Sigma}'$, with elements $\Sigma'_{11} = \Sigma'_{22} = \Sigma'_{33} = 165.7$ GPa $\Sigma'_{12} = \Sigma'_{13} = 63.9$ GPa $\Sigma'_{44} = \Sigma'_{55} = \Sigma'_{66} = 79.6$ GPa
Pz26 parameters: [42]	
Density	$\rho_{pz} = 7700$ kg m^{-3}
Stiffness matrix	$\boldsymbol{\Sigma}_{pz} = \{1 + [i(1/Q_\Sigma)]\}\boldsymbol{\Sigma}'$, with elements $\Sigma'_{11} = \Sigma'_{22} = 168$ GPa $\Sigma'_{12} = 110$ GPa, $\Sigma'_{13} = 99.9$ GPa $\Sigma'_{23} = 99.9$ GPa, $\Sigma'_{33} = 123$ GPa $\Sigma'_{44} = \Sigma'_{55} = 30.1$ GPa $\Sigma'_{66} = 28.8$ GPa
Quality factor for Σ	$Q_\Sigma = 100$
Dielectric tensor	$\boldsymbol{\varepsilon} = \{1 - [1/(Q_\varepsilon)]\}\boldsymbol{\varepsilon}$ $\varepsilon_{11} = \varepsilon_{22} = 828$ $\varepsilon_{33} = 700$
Quality factor for ε	$Q_\varepsilon = 333$
Coupling matrix	$\boldsymbol{P}_{Pz} = \{1 + [i(1/Q_{Pz})]\}\boldsymbol{P}'$, with elements $P'_{15} = P'_{24} = 9.86$ C m^{-2} $P'_{31} = P'_{32} = -2.8$ C m^{-2} $P'_{33} = 14.7$ C m^{-2}
Quality factor	$Q_{Pz} = [2Q_\Sigma Q_\varepsilon/(Q_\varepsilon - Q_\Sigma)] = 286$

resolution parameter m_{res} of between zero and unity. As illustrated in Fig. 2 for $m_{res} = 0.35$, the maximum linear size of the mesh elements is set to be $m_{res}h_{ch}$ in the channel, $0.1m_{res}h_{ch}$ at six corners, and $1.4m_{res}h_{ch}$ elsewhere. We consider the four mesh resolutions $m_{res} = 0.10, 0.14, 0.20$, and 0.35, corresponding to a doubling of the number of mesh elements for each step, then use the results for the finest mesh $m^*_{res} = 0.10$ as the reference solution. For a given field $F(f, m_{res})$, we define the mesh- and frequency-dependent relative error $\mathrm{err}[F(f, m_{res})]$ and its average $\overline{\mathrm{err}}[F(m_{res})]$ over N discrete frequencies f_k by

$$\mathrm{err}[F(f,m_{\mathrm{res}})] = \left|\frac{F(f,m_{\mathrm{res}}) - F(f,m^*_{\mathrm{res}})}{F(f,m^*_{\mathrm{res}})}\right|, \tag{26a}$$

$$\overline{\mathrm{err}}[F(m_{\mathrm{res}})] = \frac{1}{N}\sum_{n=k}^{N} \mathrm{err}[F(f_k,m_{\mathrm{res}})]. \tag{26b}$$

In Fig. 4(a), we show plots of the average relative errors of the Lagrangian L and the Hamiltonian H versus the mesh resolution m_{res} for $N = 1001$ frequencies between 1.5 and 2.5 MHz, in steps of 1 kHz. The error is below 1% for all meshes and decreases proportionally to m^2_{res} as $m_{\mathrm{res}} \to 0$. In Fig. 4(b), we plot the relative error for each of the N frequencies for a fixed mesh resolution $m_{\mathrm{mes}} = 0.14$. The relative error fluctuates as a function of frequency, with pronounced local maxima near what turns out to be resonance frequencies. The largest maximum is 5×10^{-3} at $f \simeq 1.7$ MHz, which is an order of magnitude larger than the average relative error of 3×10^{-4}, but still below 1%. To trade off between computational time and accuracy, we use the mesh resolution $m_{\mathrm{res}} = 0.14$ (yielding 150 000 degrees of freedom) in all of the numerical simulations presented here.

The internal consistency in the implementation of the governing equations and the boundary conditions has been

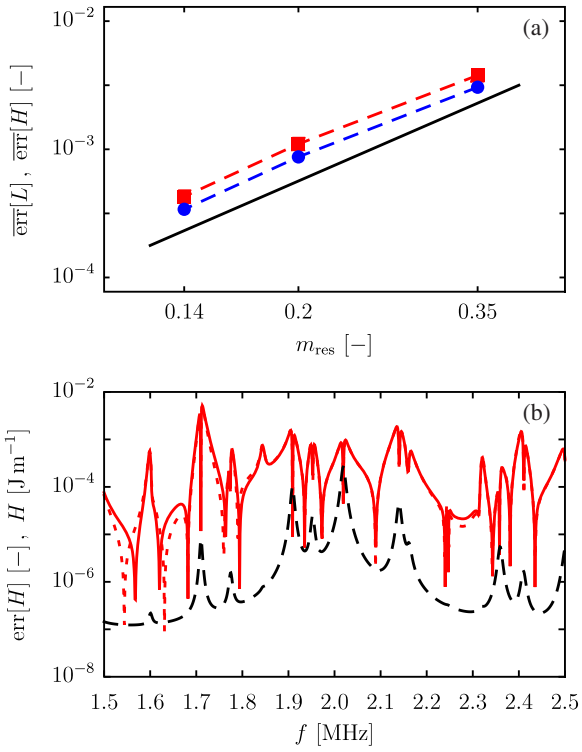

FIG. 4. (a) Log-log plot of $\overline{\mathrm{err}}[L(m_{\mathrm{res}})]$ (filled circle) and $\overline{\mathrm{err}}[H(m_{\mathrm{res}})]$ (filled square). The straight line is a reference slope corresponding to m^2_{res}. (b) Plot of the relative error for the real part (solid red line) and the imaginary part (dashed red line) of the Hamiltonian (dashed black line) for $m_{\mathrm{res}} = 0.14$.

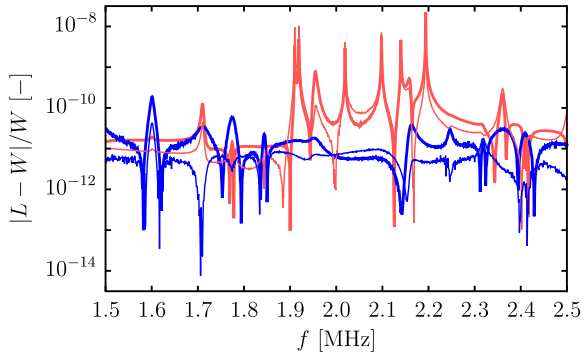

FIG. 5. Relative deviations for the real part (the light red lines) and imaginary part (the blue lines) of the Lagrangian $\hat{L}$ from the external work $\hat{W}$ versus frequency f for $d_{\mathrm{pz}} = 0$ μm, $h_{\mathrm{gl}} = 1100$ μm for two mesh resolutions: $m_{\mathrm{res}} = 0.10$ (the thin lines) and $m_{\mathrm{res}} = 0.14$ (the thick lines).

tested by using Eq. (16), which states that the total work $\hat{W}$ provided by the applied potential ϕ_{app} on the piezoelectric transducer must equal the total Lagrangian $\hat{L}$ defined in Eq. (21a). In Fig. 5, the relative deviation $|(\hat{L} - \hat{W})/\hat{W}|$ between these two quantities is plotted as a function of the actuation frequency for the two mesh resolutions $m_{\mathrm{res}} = 0.10$ and 0.14, and it is found to be numerically zero for all of the frequencies.

IV. RESULTS

Since the usual standing-half-wave resonance in the microchannel is $f_0 = [c/(2w_{\mathrm{ch}})] = 1.974$ MHz, we simulate the response of the acoustofluidic device to actuation frequencies from 1.5 to 2.5 MHz. We vary the lid height h_{gl} and the displacement d_{pz} of the piezoelectric transducer as indicated in Table I, and we study two different transparent materials for the glass lid, namely, Pyrex and the more stiff and heavy ALON [43].

A. Procedure for identifying good acoustophoresis

In experiments aiming for the separation or focusing of particles, a strong and well-oriented acoustophoretic force is necessary to provide the adequate displacement of the particle stream towards the pressure node fast enough to be completed before the particle stream leaves the device. The occurrence of a resonant state is, therefore, a necessary condition for producing a strong acoustophoretic force. In order to identify the optimal actuation frequency f for a given device geometry and applied voltage ϕ_{app}, we employ the indicators introduced in Sec. II D.

First, we locate the frequencies for which the acoustophoretic mean orientation θ, as defined in Eq. (25), exceeds a threshold value $0 < \theta_0 < 1$ close to 1. Therefore, we introduce the concept of *acoustophoretic bands* (ACP bands) as

$$\text{ACP bands} = \text{frequencies for which } \theta(f) > \theta_0. \quad (27)$$

This requirement ensures that the orientation of the pressure field and the resulting acoustic radiation force leads to microparticle migration towards a vertical nodal line, and it can be regarded as a quality measure of the acoustic force.

On the other hand, the acoustophoretic-force intensity is regulated by the amount of energy present in the channel for a specific actuation frequency. Therefore, we look for frequencies for which either the system energy H or the channel energy $H_{ch} = \eta H$ attain maxima. In the first case, the actuation frequencies correspond to resonance frequencies of the entire system, while in the second case, we demand only an amount of energy in the channel sufficient to obtain acoustophoresis. Note that channel resonances and system resonances do not need to coincide. Note also that the detection of a channel resonance is achievable only by indirect measurements, such as microparticle-image-velocimetry experiments, while the detection of a system resonance is easily achievable by means of electrical measurement—for example, by looking at the minima of the real part of the impedance.

We can now establish a numerical procedure for identifying effective actuation frequencies in terms of acoustophoresis as follows: (i) by calculating the indicators θ, η, H_{ch}, and H as a function of the frequency f in a chosen interval, (ii) by identifying the ACP bands for a threshold value, (iii) by locating within the ACP bands the frequencies f_n leading to local maxima of H, and (iv) by computing the optimal actuation frequency f_{acp}, which is defined

$$f_{acp} = f \text{ that maximizes } H_{ch} \text{ in the ACP bands.} \quad (28)$$

For comparison purposes, we also keep track of the frequency f_H for which $H(f_n)$ has a global maximum within the acoustophoretic bands.

B. Mechanical characterization

An example of the identification procedure for Pyrex-silicon devices is reported in Fig. 6. Here, θ, η, H_{ch}, and H are plotted versus the actuation frequency f in the interval from 1.5 to 2.5 MHz for all 12 combinations of glass height and piezoelectric displacement listed in Table I. For each device, the top graph contains the lin-lin plot of θ (the solid and dashed black line), while the bottom graph contains the log-lin plots of the acoustofluidic yield η (the red line), the channel energy $H_{ch}/(1\ \text{Pa})$ (the purple line), and the total energy $H/(1\ \text{Pa})$ (the blue line). We show the ACP bands for $\theta_0 = 0.95$ (the gray areas), the local maxima of the total energy within the ACP bands $H(f_n)$ (the open circles), the global maximum of the total energy within the ACP bands $H(f_H)$ (the filled circles), and, finally, the optimal frequency f_{acp} (the vertical dashed line).

Some general features can be observed in the figure. First, the ACP bands are practically absent for the symmetrically placed transducer ($d_{pz} = 0$), and the orientation θ rarely surpasses even 0.9; these responses occur because the specific transducer—that is, Pz26—is mainly characterized by a compression or extension actuation mode in the z direction [42] that, in a piezoelectric- or chip-symmetric configuration, does not provide a sufficient excitation for the y-directed vibrational modes that are those responsible for the acoustophoresis. Second, for the asymmetrically placed transducer, the width of the ACP bands increases for an increasing lid height h_{gl}. Third, we note that the optimal acoustophoretic frequency f_{acp} does not coincide with a local maximum in H for all of the cases we investigate (see the cases $d_{pz} = 250\ \mu\text{m}$, $h_{gl} = 1100\ \mu\text{m}$ and $d_{pz} = 500\ \mu\text{m}$, $h_{gl} = 200\ \mu\text{m}$). These observations point out the complex interplay between the different parts of the device and highlight the fact that the channel, where acoustophoresis is observed, is a small part of the system, and it can contain a remarkable amount of energy even when the whole system is not resonating.

C. Example of identifying good acoustophoresis

The ability to identify optimal frequencies for acoustophoresis by using the procedure introduced above is illustrated by the two examples shown in Fig. 7. The two systems have Pyrex lids and nearly identical geometries defined by the parameters listed in Table I. The piezoelectric displacement is $d_{pz} = 250\ \mu\text{m}$ in both cases, while the glass-lid height is $h_{gl} = 200\ \mu\text{m}$ [Fig. 7(a)] and $h_{gl} = 700\ \mu\text{m}$ [Fig. 7(b)]. The respective optimal actuation frequencies $f_{acp} = 1.875$ and $f_{acp} = 2.099$ MHz have been obtained by using the definition equation (28). Despite the very different displacement fields in the surrounding chip material, which is represented as the magnitude of the real part of the displacement $|\text{Re}(\boldsymbol{u})|$ by the color plot (from blue zero, via green, to red maximum), both systems exhibit a nearly perfect horizontal standing pressure wave $\text{Re}(p)$ (the color plot from blue minimum, through white, to red maximum or line plot in the inset) in the fluid. This occurrence has been observed experimentally [25–27], and it is ideal for forcing the particles to the vertical pressure nodal plane in the center of the channel. By definition of f_{acp}, the orientation θ is close to unity in both systems. In all of the cases for which we locate f_{acp} by using the identification procedure, we have observed similar behaviors in the pressure field inside the microchannel.

D. Electrical characterization

So far, the device characterization has involved only the mechanical indicators θ, H, H_{ch}, and η—which, unfortunately, cannot be measured directly and easily during the experiments. It would be advantageous if the acoustophoretic performance of a given system could be assessed by measuring only electrical quantities through the connection of the piezoelectric transducer. A good candidate

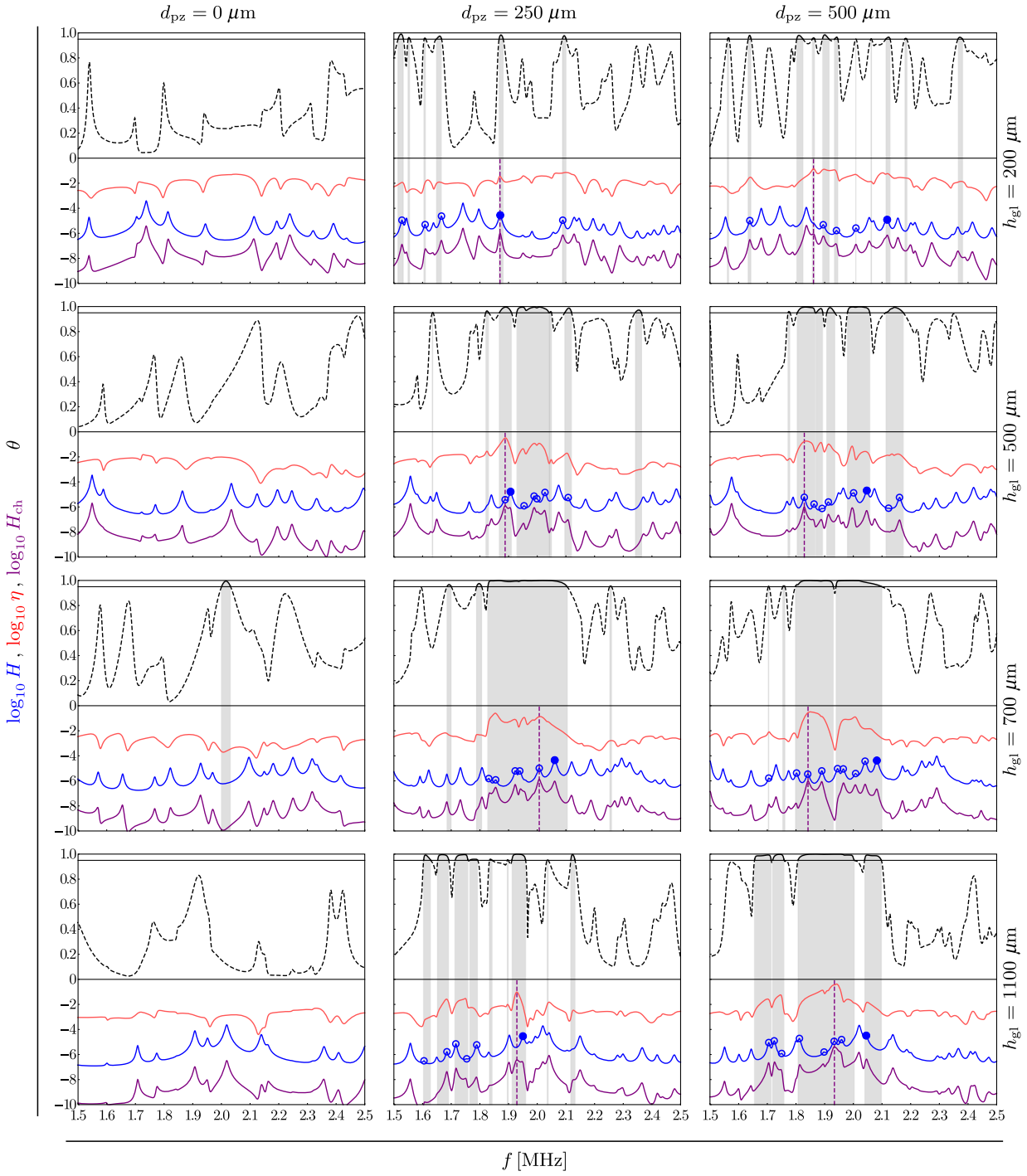

FIG. 6. Plots of the indicators versus the frequency f between 1.5 and 2.5 MHz in a Pyrex-silicon device: the acoustophoretic orientation θ (the solid and dashed black lines), the Hamiltonian H (the dark blue lines), the acoustofluidic yield η (the light red lines), and the channel energy H_{ch} (the purple line), each shown for the three positions d_{pz} (the values atop of columns) of the piezoelectric transducer and four glass heights (the values in the right-hand rows). Gray-shaded regions are the ACP-band equations (27) for $\theta = 0.95$. In the graphs, we have highlighted the local maxima in $H(f_n)$ (the empty circles), the global maximum $H(f_H)$ (the filled circles), and the optimal acoustophoretic frequency f_{acp} (the vertical dashed lines).

for an easily accessible indicator is the complex-valued electrical impedance $\hat{Z} = Ze^{i\varphi_Z}$ in Eq. (22), which can be measured experimentally with the use of an impedance analyzer. This frequency-dependent complex-valued indicator can be written as $\hat{Z} = R + iX$, where the real part R is the resistance and the imaginary part X is the reactance. A system is considered to behave inductively for $X > 0$ (or $0 < \varphi_Z < (\pi/2)$) and capacitively for $X < 0$ (or

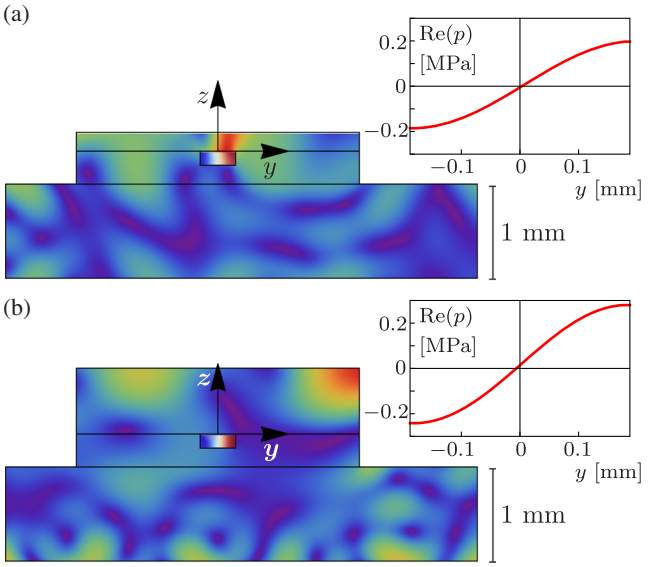

FIG. 7. Color plot of the magnitude $|\mathrm{Re}(\boldsymbol{u})|$ of the real part of the displacement field in the solids (the rainbow color map) and the real part $\mathrm{Re}(p)$ of the acoustic pressure in the fluid (the red-white-and-blue color map) for two silicon-Pyrex devices with (a) $h_{\mathrm{gl}}=200\,\mu$m at $f=f_{\mathrm{acp}}=1.875$ MHz, and (b) $h_{\mathrm{gl}}=700\ \mu$m at $f=f_{\mathrm{acp}}=2.099$ MHz. (Insets) The real part $\mathrm{Re}(p)$ of the pressure along the horizontal centerline of the water-filled microchannel.

$-(\pi/2)<\varphi_Z<0$). Depending on the internal structure of the electric circuit (*RLC* series or parallel), driving the system at the resonance frequency can amplify voltage or current [38]. This response occurs for zero reactance when the system is purely resistive, and the current is in phase with the applied voltage. In this situation, the magnitude of the impedance can be at either a local minimum or a local maximum, and the system is said to be in a resonant or antiresonant state, respectively. Driving the device at a resonance frequency, leads to a local maximum of stored energy H, and this value can be large even for a low input power.

In Fig. 8, we show the frequency dependence of the magnitude Z [top row; unit Ωm, as this is a two-dimensional (2D) calculation] and the phase φ_Z (bottom row) of the electrical impedance $\hat{Z}$ for silicon-Pyrex devices with lid heights $h_{\mathrm{gl}}=200\ \mu$m (first column) and 1100 μm (second column) and three different displacements of the piezoelectric transducer, $d_{\mathrm{pz}}=0\ \mu$m (the red lines), 250 μm (the green lines), and 500 μm (the blue lines). The response of the system alternates between resonances and antiresonances (minima and maxima in the impedance while the phase crosses zero), but, for the chosen parameters, the system has a prevalent capacitive behavior ($\varphi_Z<0$) with intermittent inductive behavior ($\varphi_Z>0$). We observe that in the cases shown in Figs. 8(a1) and 8(a2) for the smaller chip, where the piezoelectric transducer is weakly loaded, the impedance exhibits many small fluctuations as a function of frequency and is sensitive to the off-center position of the piezoelectric transducer. For the larger chip cases shown in Figs. 8(b1) and 8(b2), less fluctuation and less sensitivity to d_{pz} is observed: the impedance and the phase curves are nearly independent of d_{pz} and the resonance frequencies nearly coincide, as do those of the antiresonances. These plots confirm the picture regarding the complicated interactions between the different parts of the system and the great sensitivity of the resonance conditions to the possible geometric configurations for the system.

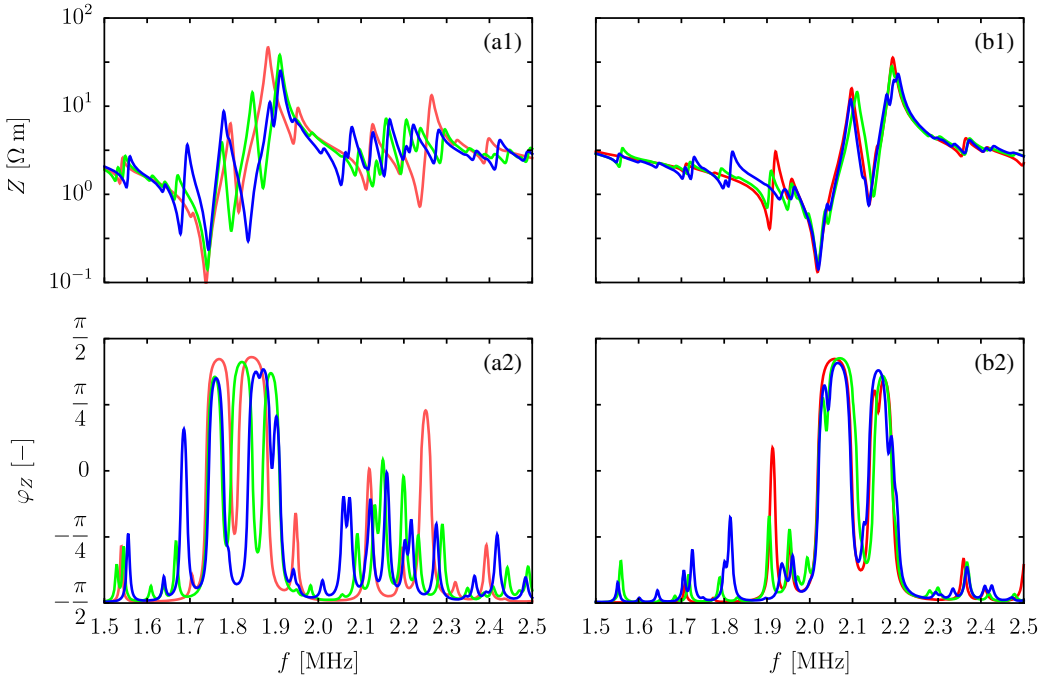

FIG. 8. Magnitude Z and phase φ_Z of the electric impedance as a function of the frequency f for Pyrex-silicon devices with three different off-center displacements of the piezoelectric transducer: $d_{\mathrm{pz}}=0\,\mu$m (the red lines), 250 μm (the green lines), and 500 μm (the blue lines). (a1), (a2) Z and φ_Z, respectively, for devices with lid thickness $h_{\mathrm{gl}}=200\ \mu$m. (b1), (b2) Z and φ_Z, respectively, for devices with lid thickness $h_{\mathrm{gl}}=1100\ \mu$m.

E. Procedure for identifying resonances from electrical impedance

Alongside these qualitative comments, it is important to establish to what extent a criterion based on the electrical-impedance characteristics can identify good acoustophoresis frequencies. It is not possible *a priori* to provide a criterion to detect frequencies (resonance or antiresonance) leading to a high energy content for the system. Instead, we try to establish empirical rules through a direct comparison of the mechanical indicators to the electrical impedance.

In Fig. 9, four prototypical cases observed in the behavior of the mechanical and electrical indicators are illustrated. The weakly loaded piezoelectric transducer (the smallest height of the lid) is shown in Fig. 9(a1). Here, a situation corresponding to a classical resonance condition for a *RLC* series circuit ($\varphi_Z = 0$ and $Z = \min$) is illustrated, and the optimal acoustophoretic frequency coincides with the frequency at which H attains a maximum, that is, $f_{\rm acp} = f_H$. This case is different than the behavior observed for the same system but for a generic resonance $f_n \neq f_{\rm acp}$ [Fig. 9(a2)], where the resonance frequency is between a maximum in the phase and a minimum in the impedance magnitude. The extremum in the phase is a maximum because the system mostly behaves as a capacitor ($\varphi_Z < 0$) and, combined with the magnitude of the impedance and the phase, it has the effect of minimizing the resistive part of the impedance, thus minimizing the power input. This phenomenology can also be observed for the other generic resonance, $f_n \neq f_{\rm acp}$ (even outside the ACP bands), in the case where the piezoelectric transducer is heavily loaded Fig. 9(b2), namely, for $h_{\rm gl} = 1100$ μm. Analogous behavior has been observed, but less frequently when the phase attains a positive maximum.

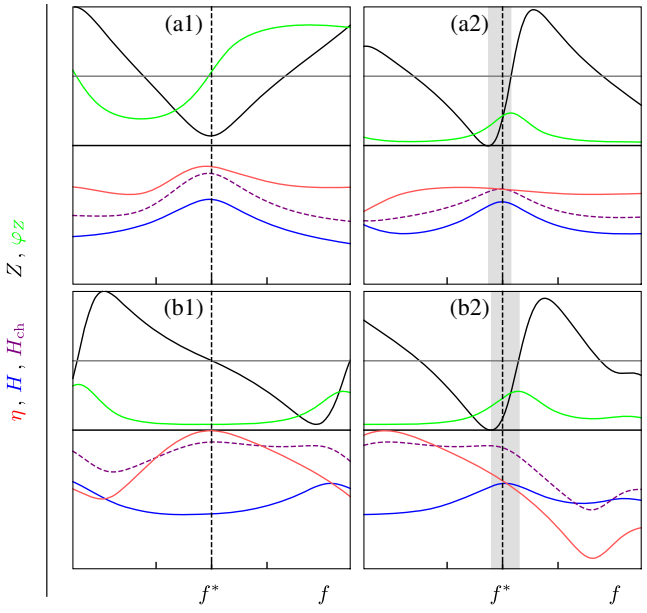

FIG. 9. The magnitude Z (black line, arbitrary scale) and the phase φ_Z (green line, thin horizontal line $\varphi_Z = 0$) of the impedance $\hat{Z}$, the energy H (blue line, arbitrary scale), the yield η (red line, arbitrary scale), and the channel energy $H_{\rm ch}$ (purple line, arbitrary scale) as a function of frequency f in an interval characterized by $\Delta f = 10$ kHz around a frequency f^* at which the channel energy is a maximum. (a1) Chip with $h_{\rm gl} = 200$ μm, $d_{\rm pz} = 250$ μm, and $f^* = f_n = f_{\rm acp} = 1.870$ MHz. (a2) Same as (a1), but at $f^* = f_n = 1.666$ MHz. (b1) Chip with $h_{\rm gl} = 1100$ μm, $d_{\rm pz} = 250$ μm, and $f^* = f_{\rm acp} = 1.929$ MHz. (b2) Same as (b1) but at $f^* = f_n = 1.950$ MHz. The gray area is the interval between the frequencies given by Eq. (29) [case (b1) cannot be detected].

Finally, quite peculiar behavior is observed for the heavily loaded piezoelectric transducer [Fig. 9(b1)] when $f = f_{\rm acp}$ but $f \neq f_n$. In this case, there is no evidence for a resonance in the system, a zero maximum in the phase, or a minimum in the impedance, while the energy content in the channel has a maximum. The pairing of this observation with the analysis of the energy quantification in Fig. 9 reveals that, in this situation, the channel energy is slightly higher than that achievable for the resonance frequency $f_n = 1.950$ MHz because the yield is quite high. This peculiar case can be seen as a case in which the channel is resonating while the whole system is not, and it is the most difficult to detect electrically since there is no trace of the energy content of the channel in the impedance measurements.

Based on these observations, a criterion for detecting resonance frequencies $f_{Z,n}$ for the system can be constructed as follows:

$$\begin{aligned} &f_{Z,n} \text{ is in the interval between } f_Z \text{ and } f_{\varphi_Z}, \text{ where} \\ &\text{(i) } f_Z = \tilde{f}, \tilde{f} \text{ minimizes } Z, \text{ and} \\ &\text{(ii) } f_{\varphi_Z} = \tilde{f} \begin{cases} \text{either } \varphi_Z(\tilde{f}) = 0 \text{ and } \varphi_Z{}'(\tilde{f}) > 0 \\ \text{or minimizes } |\varphi_Z(\tilde{f})|. \end{cases} \end{aligned} \tag{29}$$

Note that this criterion is a less restrictive version of the criterion used to detect resonance frequencies for a *RLC*-series circuit, equipped with the additional condition that the phase attains a negative maximum or a positive minimum. The criterion equation (29) does not provide the location for an exact resonance frequency of the system, but it addresses a frequency interval in which it is possible to find the resonance frequency. The intervals are formally given by $f_Z < f_{Z,n} < f_{\varphi_Z}$ and $f_{\varphi_Z} < f_{Z,n} < f_Z$ for $\varphi_Z < 0$ and $\varphi_Z > 0$, respectively. As shown in the figure, these frequency intervals are quite narrow and, for the classical resonance conditions $\varphi_Z = 0$, the frequency bounds coincide and a single frequency is recovered.

Figure 10 reports the results of the application of the criterion equation (29) to the detection of resonance frequency intervals for two silicon-glass devices, with $d_{\rm pz} = 250\,\mu$m for (a) $h_{\rm gl} = 200$ μm and (b) $h_{\rm gl} = 1100$ μm,

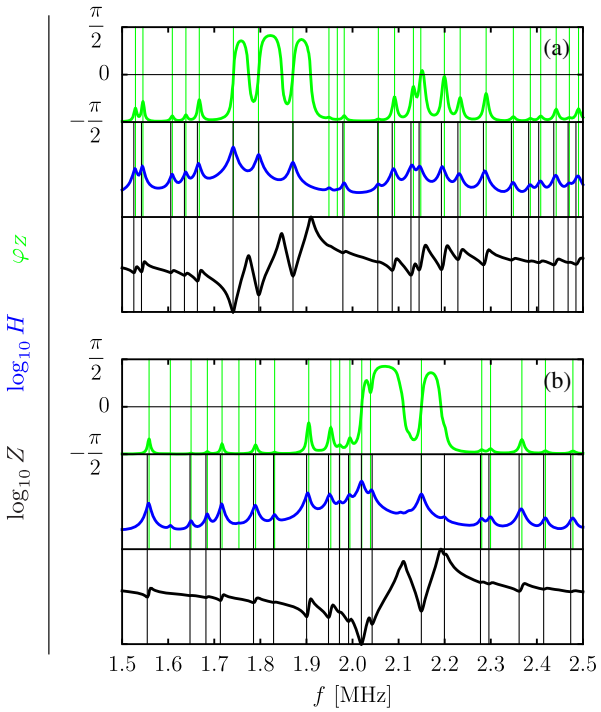

FIG. 10. Phase φ_Z (green lines), impedance Z (black lines), and energy H (blue lines) as function of the frequency f for Pyrex-silicon devices with $d_{pz} = 250$ μm for (a) $h_{gl} = 200$ μm and (b) $h_{gl} = 1100$ μm. Vertical black and green lines mark the frequencies obtained via the criterion equations (29)(i) and (29)(ii), respectively.

by depicting the spectral behavior of the phase φ_Z (top plot), the energy H (center plot), and the impedance $|\hat{Z}|$ (bottom plot). The green and black vertical lines mark the frequency bounds obtained through Eq. (29) by applying criteria (i) and (ii), respectively. Here, the effectiveness of the criterion equation (29) in the detection of frequency intervals containing resonance frequencies can be appreciated. Indeed, in almost all of the cases, the energy maxima are enclosed in the predicted intervals. It can also be observed that when one of the two criteria is missing (mostly because of the procedure used in the extremum calculation over numerical data), the other can still provide a good approximation for the resonance frequencies. Although the criterion equation (29) can detect resonance frequencies for the system, the effectiveness of these frequencies in producing particle focusing is still hidden by the fact that the impedance indicates an overall performance of the system and does not contain information about the orientation of the pressure wave in the microchannel.

V. CONCLUSION

In this work, the Helmholtz equations governing the elastic, acoustic, and piezoelectric waves in an acoustophoretic device are formulated in terms of the free Lagrangian densities of each subsystem: the piezoelectric transducer, the silicon substrate, the glass lid, and the water-filled microchannel. The subsystems are coupled and boundary conditions are imposed by adding surface contributions to the free Lagrangian densities. In this way, we construct a consistent model that takes the coupling between the different subsystems and the electric actuation into account. The model is implemented and thoroughly tested by means of numerical simulations by using a weak-form implementation in the commercial software COMSOL Multiphysics, version 4.4a.

Three frequency-dependent mechanical indicators are introduced to characterize the acoustophoretic response of the system: the total energy H, the acoustofluidic yield η, and the mean acoustophoretic orientation θ. A specific procedure that allows for the identification of optimal frequencies f_{acp} is provided so that it is possible to obtain good acoustophoretic focusing of suspended microparticles flowing through the microchannel. Additional electrical indicators, such as the impedance $\hat{Z}$ of the system, the power input P, and the Q value are correlated with the Lagrangian and the Hamiltonian of the system.

We (i) illustrate the general guidelines for obtaining optimal actuation frequencies f_{acp} from a spectral analysis of the mechanical indicators and (ii) by comparing mechanical and electric indicators, we provide an empirical criterion for detecting resonance frequencies (high energy in the system) by using impedance characteristics.

To exemplify the use of the present model as a possible design tool, we analyze variations in the spectral behavior induced by changing the commonly used glass lid from Pyrex to ALON [43]. The analysis reveals unique features of ALON, such as stabilization of the optimal resonance frequency as the height of the lid increases. This behavior deserves further experimental studies employing other stiff materials, such as sapphire [44], for which some perspectives on the bonding process are known [45]. The rule equation (29) based on the comparative analysis of the mechanical and electrical characteristics of the device is easy to implement in the applications, and it can successfully predict the frequency ranges in which system resonances occur.

In summary, the model we report may be employed (i) as an optimal design tool in the future development of acoustophoretic devices or (ii) to narrow experimental frequency intervals for the detection of optimal resonance frequencies by using optical techniques. It demonstrates the effectiveness of the employment of basic theories in the area of coupled mechanical and electrical systems and, as such, is closely related to the developments in mechatronics [46,47], and it points towards the possibility of reducing the expensive and time-consuming trial-and-error fabrication procedures presently being used in the field.

ACKNOWLEDGMENTS

This work was supported by the Knut and Alice Wallenberg Foundation (Grant No. KAW 2012.0023).

APPENDIX: AXIAL MODES ANALYSIS

For completeness, we use an analysis of the axial modes to briefly discuss the connection between the 2D model presented in the manuscript and a full three-dimensional (3D) model. Table III contains the symbols used here as well as in the main text.

Using the combined variable $\boldsymbol{q} = [\boldsymbol{u}, p, \phi]^T$, the governing equations (3), (5), and (7a) can be obtained from the Euler-Lagrange equation with the Lagrangian density

$$\mathcal{L}(\boldsymbol{q}, \boldsymbol{\nabla q}) = \boldsymbol{q}^\dagger \mathbf{K} \boldsymbol{q} + (\boldsymbol{\nabla q})^\dagger \mathbf{M} \boldsymbol{\nabla q}, \tag{A1}$$

TABLE III. Summary of symbols and their meanings. Scalars are addressed by means of plain roman and greek letters. Script symbols refer to Lagrangian, Hamiltonian, work, and power densities. Vectors and tensors of second, third, and fourth ranks are addressed by using bold roman, bold greek, bold capital roman, and bold capital greek, respectively. Primed symbols address the Voigt notation for the symmetrizable tensors.

Rank	Symbol	Description	Units
0	f	frequency	Hz
	ω	angular frequency	rad/s
	ρ	density	kg/m^3
	E	Young modulus	N/m^2
	ν	Poisson ratio	1
	p	pressure	Pa
	ϕ	electric potential	V
	$\mathcal{L}$	Lagrangian density	J/m^3
	$\mathcal{H}$	Hamiltonian density	J/m^3
	$\mathcal{W}$	work density	J/m^3
	$\mathcal{P}$	power density	J/sm^3
	L	Lagrangian	J
	H	Hamiltonian	J
	W	work	J
	P	electric power	J/s
	Z	electric impedance	Ω
	I	electric current	A
	η	acoustofluidic yield	1
	θ	acoustophoretic orientation	1
1	$\boldsymbol{u}$	displacement	m
	$\boldsymbol{v}$	velocity	m/s
	$\boldsymbol{a}$	acceleration	m/s^2
	$\boldsymbol{d}$	electric displacement	C/m^2
	$\hat{\boldsymbol{n}}$	outward normal	1
2	1	unit tensor	1
	$\boldsymbol{\varepsilon}$	dielectric tensor	F/m^2
	$\boldsymbol{\gamma}$	strain $\frac{1}{2}(\nabla \boldsymbol{u} + \boldsymbol{u}\nabla)$	1
	$\boldsymbol{\sigma}$	stress	N/m^2
3	$\boldsymbol{P}$	electric-field strain piezoelectric coupling	C/m^2
4	$\boldsymbol{\Sigma}$	stiffness tensor	N/m^2

where $\boldsymbol{q}^\dagger = (\boldsymbol{q}^*)^T$, $\boldsymbol{q}^\dagger \boldsymbol{q}$ is the inner product for the space of the complex-valued states, $\mathbf{K}$ is a matrix with scalar entries

$$\mathbf{K} = \begin{pmatrix} \rho\omega^2 & 0 & 0 \\ 0 & -\kappa_s & 0 \\ 0 & 0 & 0 \end{pmatrix}, \tag{A2}$$

and $\mathbf{M}$ is a matrix with tensorial entries

$$\mathbf{M} = \begin{pmatrix} \boldsymbol{\Sigma} & 0 & -\boldsymbol{P} \\ 0 & (\rho\omega^2)^{-1} & 0 \\ -\boldsymbol{P}^T & 0 & \boldsymbol{\varepsilon} \end{pmatrix}. \tag{A3}$$

Let the position coordinate be written as $\boldsymbol{r} = (x, \boldsymbol{r}_\perp)$, such that x is the axial coordinate and $\boldsymbol{r}_\perp = (y, z)$ are the cross-section coordinates. We assume that the device is axially periodic along the x axis with period ℓ so that $0 < x < \ell$ and $\boldsymbol{q}(0, \boldsymbol{r}_\perp, \omega) = \boldsymbol{q}(\ell, \boldsymbol{r}_\perp, \omega)$. Using a discrete Fourier series in the axial coordinate, we can write

$$\boldsymbol{q}(x, \boldsymbol{r}_\perp, \omega) = \sum_{n=-\infty}^{\infty} \hat{\boldsymbol{q}}_n(\boldsymbol{r}_\perp, \omega) e^{i2\pi n x/\ell}, \tag{A4}$$

where the amplitudes $\hat{\boldsymbol{q}}_n$ are given by

$$\hat{\boldsymbol{q}}_n(\boldsymbol{x}_\perp, \omega) = \frac{1}{\ell} \int_{-\ell/2}^{\ell/2} \boldsymbol{q}(\boldsymbol{x}_\perp, \omega) e^{-i2\pi n x/\ell} dx. \tag{A5}$$

The nabla operator $\hat{\boldsymbol{\nabla}}$ acting on $\hat{\boldsymbol{q}}$ is written as

$$\hat{\boldsymbol{\nabla}} = i\frac{2\pi n}{\ell} \boldsymbol{e}_x + \boldsymbol{\nabla}_\perp, \tag{A6}$$

where $\boldsymbol{\nabla}_\perp = \boldsymbol{e}_y \partial_y + \boldsymbol{e}_z \partial_z$ is the cross-section nabla operator. Since the quadratic Lagrangian density (A1) leads to linear equations of motion, the axial-mode decomposition of any solution $\boldsymbol{q}$ is unique and complete, and each of the axial modes $\hat{\boldsymbol{q}}_n$ can be determined from their respective Lagrangian densities,

$$\mathcal{L}_n(\hat{\boldsymbol{q}}_n, \hat{\nabla}\hat{\boldsymbol{q}}_n) = \hat{\boldsymbol{q}}_n^\dagger \mathbf{K} \hat{\boldsymbol{q}}_n + (\hat{\nabla}\hat{\boldsymbol{q}}_n)^\dagger \mathbf{M} \hat{\nabla} \hat{\boldsymbol{q}}_n. \tag{A7}$$

This splitting is possible because $\mathbf{M}$ and $\mathbf{K}$ do not depend on the spatial coordinates.

For the axially invariant mode $n = 0$, there is no dependence on x and $\hat{\boldsymbol{\nabla}} = \boldsymbol{\nabla}_\perp$. Moreover, the displacement field is restricted to be in the cross section, $\boldsymbol{u} \cdot \boldsymbol{e}_x = 0$. Consequently, the Lagrangian density $\mathcal{L}_0$ for the $n = 0$ mode can be written as

$$\mathcal{L}_0(\hat{\boldsymbol{q}}_0, \boldsymbol{\nabla}_\perp \hat{\boldsymbol{q}}_0) = \hat{\boldsymbol{q}}_0^\dagger \mathbf{K} \hat{\boldsymbol{q}}_0 + (\boldsymbol{\nabla}_\perp \hat{\boldsymbol{q}}_0)^\dagger \mathbf{M}_\perp \boldsymbol{\nabla}_\perp \hat{\boldsymbol{q}}_0, \tag{A8}$$

where $\mathbf{M}_\perp$ contains only the tensorial components in the cross-section plane from $\mathbf{M}$. This Lagrangian density

directly leads to 2D equations of motion with the bulk-material properties studied in Sec. II. In an extended treatment, the axial modes can be used to approach a full 3D solution by taking higher modes with $|n| > 0$ into account.

[1] Henrik Bruus, Acoustofluidics 7: The acoustic radiation force on small particles, Lab Chip **12**, 1014 (2012).

[2] Mikkel Settnes and Henrik Bruus, Forces acting on a small particle in an acoustical field in a viscous fluid, Phys. Rev. E **85**, 016327 (2012).

[3] Jonas T. Karlsen and Henrik Bruus, Forces acting on a small particle in an acoustical field in a thermoviscous fluid, Phys. Rev. E **92**, 043010 (2015).

[4] Henrik Bruus, Jürg Dual, Jeremy Hawkes, Martyn Hill, Thomas Laurell, Johan Nilsson, Stefan Radel, Satwindar Sadhal, and Martin Wiklund, Forthcoming lab on a chip tutorial series on acoustofluidics: Acoustofluidics—Exploiting ultrasonic standing wave forces and acoustic streaming in microfluidic systems for cell and particle manipulation, Lab Chip **11**, 3579 (2011).

[5] Miguel A. Burguillos, Cecilia Magnusson, Maria Nordin, Andreas Lenshof, Per Augustsson, Magnus J. Hansson, Eskil Elmér, Hans Lilja, Patrik Brundin, Thomas Laurell, and Tomas Deierborg, Microchannel acoustophoresis does not impact survival or function of microglia, leukocytes or tumor cells, PLoS One **8**, e64233 (2013).

[6] Martin Wiklund, Acoustofluidics 12: Biocompatibility and cell viability in microfluidic acoustic resonators, Lab Chip **12**, 2018 (2012).

[7] Maria Nordin and Thomas Laurell, Two-hundredfold volume concentration of dilute cell and particle suspensions using chip integrated multistage acoustophoresis, Lab Chip **12**, 4610 (2012).

[8] Mikael Evander and Johan Nilsson, Acoustofluidics 20: Applications in acoustic trapping, Lab Chip **12**, 4667 (2012).

[9] Per Augustsson and Thomas Laurell, Acoustofluidics 11: Affinity specific extraction and sample decomplexing using continuous flow acoustophoresis, Lab Chip **12**, 1742 (2012).

[10] O. Manneberg, J. Svennebring, H. M. Hertz, and M. Wiklund, Wedge transducer design for two-dimensional ultrasonic manipulation in a microfluidic chip, J. Micromech. Microeng. **18**, 095025 (2008).

[11] Per Augustsson, Cecilia Magnusson, Maria Nordin, Hans Lilja, and Thomas Laurell, Microfluidic, label-free enrichment of prostate cancer cells in blood based on acoustophoresis, Anal. Chem. **84**, 7954 (2012).

[12] X. Ding, Z. Peng, S.-C. S. Lin, M. Geri, S. Li, P. Li, Y. Chen, M. Dao, S. Suresh, and T. J. Huang, Cell separation using tilted-angle standing surface acoustic waves, Proc. Natl. Acad. Sci. U.S.A. **111**, 12992 (2014).

[13] Filip Petersson, Lena Åberg, Ann-Margret Swärd-Nilsson, and Thomas Laurell, Free flow acoustophoresis: Microfluidic-based mode of particle and cell separation, Anal. Chem. **79**, 5117 (2007).

[14] Björn Hammarström, Mikael Evander, Jacob Wahlström, and Johan Nilsson, Frequency tracking in acoustic trapping for improved performance stability and system surveillance, Lab Chip **14**, 1005 (2014).

[15] James Friend and Leslie Y. Yeo, Microscale acoustofluidics: Microfluidics driven via acoustics and ultrasonics, Rev. Mod. Phys. **83**, 647 (2011).

[16] Jurg Dual and Thomas Schwarz, Acoustofluidics 3: Continuum mechanics for ultrasonic particle manipulation, Lab Chip **12**, 244 (2012).

[17] Jurg Dual and Dirk Möller, Acoustofluidics 4: Piezoelectricity and application in the excitation of acoustic fields for ultrasonic particle manipulation, Lab Chip **12**, 506 (2012).

[18] P. B. Muller, M. Rossi, Á. G. Marín, R. Barnkob, P. Augustsson, T. Laurell, C. J. Kähler, and H. Bruus, Ultrasound-induced acoustophoretic motion of microparticles in three dimensions, Phys. Rev. E **88**, 023006 (2013).

[19] Peter Barkholt Muller and Henrik Bruus, Numerical study of thermoviscous effects in ultrasound-induced acoustic streaming in microchannels, Phys. Rev. E **90**, 043016 (2014).

[20] Peter Barkholt Muller and Henrik Bruus, Theoretical study of time-dependent, ultrasound-induced acoustic streaming in microchannels, Phys. Rev. E **92**, 063018 (2015).

[21] Philipp Hahn, Olivier Schwab, and Jürg Dual, Modeling and optimization of acoustofluidic micro-devices, Lab Chip **14**, 3937 (2014).

[22] A. Neild, S. Oberti, and J. Dual, Design, modeling and characterization of microfluidic devices for ultrasonic manipulation, Sens. Actuators B **121**, 452 (2007).

[23] Stefano Oberti, Adrian Neild, Dirk Möller, and Jürg Dual, Towards the automation of micron-sized particle handling by use of acoustic manipulation assisted by microfluidics, Ultrasonics **48**, 529 (2008).

[24] Peter Barkholt Muller, Rune Barnkob, Mads Jakob Herring Jensen, and Henrik Bruus, A numerical study of microparticle acoustophoresis driven by acoustic radiation forces and streaming-induced drag forces, Lab Chip **12**, 4617 (2012).

[25] Rune Barnkob, Per Augustsson, Thomas Laurell, and Henrik Bruus, Measuring the local pressure amplitude in microchannel acoustophoresis, Lab Chip **10**, 563 (2010).

[26] Per Augustsson, Rune Barnkob, Steven T. Wereley, Henrik Bruus, and Thomas Laurell, Automated and temperature-controlled micro-PIV measurements enabling long-term-stable microchannel acoustophoresis characterization, Lab Chip **11**, 4152 (2011).

[27] Rune Barnkob, Per Augustsson, Thomas Laurell, and Henrik Bruus, Acoustic radiation- and streaming-induced microparticle velocities determined by microparticle image velocimetry in an ultrasound symmetry plane, Phys. Rev. E **86**, 056307 (2012).

[28] Jonathan D. Adams, Christian L. Ebbesen, Rune Barnkob, Allen H. J. Yang, H. Tom Soh, and Henrik Bruus, High-throughput, temperature-controlled microchannel acoustophoresis device made with rapid prototyping, J. Micromech. Microeng. **22**, 075017 (2012).

[29] Surmet, http://www.surmet.com (2015).

[30] L. D. Landau, *Theory of Elasticity 7* (Elsevier, Oxford, 2004).

[31] Karl F. Graff, *Wave Motion in Elastic Solids* (Dover Publications, New York, 1991).
[32] P. C. Chou and M.Ed. Pagano, *Elasticity: Tensor, Dyadic, and Engineering Approaches* (Dover Publications, New York, 1992).
[33] B. L. Moiseiwitsch, *Variational Principles* (Dover Publications, New York, 2004).
[34] Philip McCord Morse and K. U. Ingard, *Theoretical Acoustics* (Princeton University Press, Princeton, NJ, 1987).
[35] Herbert Goldstein, Charles P. Poole, Jr., and John L. Safko, *Classical Mechanics*, 3rd ed. (Pearson, London, 2001).
[36] Buye Xu, Scott D. Sommerfeldt, and Timothy W. Leishman, Generalized acoustic energy density, J. Acoust. Soc. Am. **130**, 1370 (2011).
[37] Qinghua Qin, *Advanced Mechanics of Piezoelectricity* (Springer, New York, 2012).
[38] James W. Nilsson and Susan Riedel, *Electric Circuits* (Prentice-Hall, Englewood Cliffs, NJ, 2014).
[39] COMSOL Multiphysics 4.4, http://www.comsol.com (2013).
[40] SCHOTT North America, http://www.schott.com (2015).
[41] Matthew A. Hopcroft, William D. Nix, and Thomas W. Kenny, What is the Young's modulus of silicon?, J. Microelectromech. Syst. **19**, 229 (2010).
[42] Ferroperm Piezoceramics, http://www.ferroperm-piezo.com (2015).
[43] See Supplemental Material at http://link.aps.org/supplemental/10.1103/PhysRevApplied.7.054026 for simulation results for ALON-silicon devices.
[44] W. C. Oliver and G. M. Pharr, An improved technique for determining hardness and elastic modulus using load and displacement sensing indentation experiments, J. Mater. Res. **7**, 1564 (1992).
[45] H. M. Manasevit and W. I. Simpson, Single-crystal silicon on a sapphire substrate, J. Appl. Phys. **35**, 1349 (1964).
[46] A. Preumont, *Mechatronics* (Springer, New York, 2006).
[47] Arno Lenk, Rüdiger G. Ballas, Günther Pfeifer, and Roland Werthschützky, *Electromechanical Systems in Microtechnology and Mechatronics* (Springer, New York, 2012).